

University of Massachusetts Amherst

ScholarWorks@UMass Amherst

Civil and Environmental Engineering Faculty
Publication Series

Civil and Environmental Engineering

2021

Surface Runoff Responses to Suburban Growth: An Integration of Remote Sensing, GIS, and Curve Number

Khurshid Jahan




Soni M. Pradhanang

Md Abul Ehsan Bhuiyan

Follow this and additional works at: https://scholarworks.umass.edu/cee_faculty_pubs

Article

Surface Runoff Responses to Suburban Growth: An Integration of Remote Sensing, GIS, and Curve Number

Khurshid Jahan ¹, Soni M. Pradhanang ^{1,*} and Md Abul Ehsan Bhuiyan ²

¹ Department of Geosciences, University of Rhode Island, South Kingston, RI 02881, USA; khurshidjahan@uri.edu

² Department of Civil and Environmental Engineering, University of Massachusetts, Amherst, MA 02115, USA; mdabulehsan@umass.edu

* Correspondence: spradhanang@uri.edu

Abstract: Suburban growth and its impacts on surface runoff were investigated using the soil conservation service curve number (SCS-CN) model, compared with the integrated advanced remote sensing and geographic information system (GIS)-based integrated approach, over South Kingston, Rhode Island, USA. This study analyzed and employed the supervised classification method on four Landsat images from 1994, 2004, 2014, and 2020 to detect land-use pattern changes through remote sensing applications. Results showed that 68.6% urban land expansion was reported from 1994 to 2020 in this suburban area. After land-use change detection, a GIS-based SCS-CN model was developed to examine suburban growth and surface runoff estimation. The developed model demonstrated the spatial distribution of runoff for each of the studied years. The results showed an increasing spatial pattern of 2% to 10% of runoff from 1994 to 2020. The correlation between runoff co-efficient and rainfall indicated the significant impact of suburban growth in surface runoff over the last 36 years in South Kingstown, RI, USA, showing a slight change of forest (8.2% area of the total area) and agricultural land (4.8% area of the total area). Suburban growth began after 2000, and within 16 years this land-use change started to show its substantial impact on surface runoff. We concluded that the proposed integrated approach could classify land-use and land cover information to understand suburban growth and its potential impact on the area.

Keywords: urbanization; suburban growth; land-use and land cover



Citation: Jahan, K.; Pradhanang, S.M.; Bhuiyan, M.A.E. Surface Runoff Responses to Suburban Growth: An Integration of Remote Sensing, GIS, and Curve Number. *Land* **2021**, *10*, 452. <https://doi.org/10.3390/land10050452>

Academic Editors: Md. Shahinoor Rahman, Mohammed Sarfaraz Gani Adnan and Steven Louis Rubinyi

Received: 12 March 2021

Accepted: 20 April 2021

Published: 23 April 2021

Publisher's Note: MDPI stays neutral with regard to jurisdictional claims in published maps and institutional affiliations.



Copyright: © 2021 by the authors. Licensee MDPI, Basel, Switzerland. This article is an open access article distributed under the terms and conditions of the Creative Commons Attribution (CC BY) license (<https://creativecommons.org/licenses/by/4.0/>).

1. Introduction

Urbanization and suburban growth increase challenges to the surface water bodies, including flooding, channel erosion, water quality degradation, biodiversity, and climate [1,2]. The current global environmental change pattern based on land use and land cover is of concern [3]. Urbanization, particularly uncontrolled expansion associated with urban sprawl, is fueled by population growth and increasing demand for residential areas. Most notably in the environmental sector, rapid urbanization degrades watershed functions and reduces agricultural and forest lands [3–5]. Eventually, the quick changes in land-use and land cover impact the annual water balance locally and, potentially, regionally [6–8], with severe consequences on the frequency, volume, and peak rates of surface runoff. The proportion of rainfall that becomes surface runoff increases along with increases in imperviousness of a watershed. Infrastructural developments such as building construction, residential development, lack of green areas, and impervious surfaces such as parking lots accelerate runoff [9]. An increase in impervious surfaces and built-up land is more vulnerable to flooding than the surrounding environment. Higher runoff volumes lead to increased occurrences of flood and expansion of floodplains. Therefore, land-use changes associated with urban development, vegetation, and hydrologic conditions are the major factors that affect urban flooding in many ways [10], leading to environmental degradation [8,11].

Recent investigations have focused on characterizing land-use changes and their adverse effects on landscape characteristics that generate flood hazards, including inundation and erosion [11]. Therefore, information on land-use and land cover (LULC), which greatly influence hydrologic applications and water quality [12–14], aids in fully understanding urbanization and its impact on local hydrology and water quality [15,16].

Urban growth has various stages, and each stage affects local hydrology in different ways [8–14]. For example, during the first stage of urbanization, hydrology is changed due to the removal of trees and vegetation [14,17], leading to decreased interception, evapotranspiration, and sedimentation. During the second stage of urbanization, houses, commercial buildings, streets, culverts, and parking lots increase imperviousness, thereby, affecting and changing the water balance. Specifically, this stage increases storm flows and runoff depth and degrades surface and groundwater quantity and quality in urban and suburban areas. The decrease in infiltration often leads to increased runoff flashiness and peak discharge for even small-sized storms. As a result, flood and waterlogging become a significant concern for highly and moderately urbanized and suburban areas. The combination of a remote sensing (RS) and a geographic information system (GIS) approach can viably assess such hydrologic changes [18–22] and produce a LULC detection map for assessing the detailed changes in an area [23]. RS has made an immense contribution to detecting change in the LULC which has helped researchers to think about the impact of LULC modifications [23,24].

Remote sensing (RS) data products are cost-effective and readily available as inputs to hydrologic and watershed models [25–27]. The RS technique gathers multispectral, multiresolution, and multitemporal data or images and then transforms the images into information for urban land-cover datasets [7]. Multispectral bands play a vital role in numerous urban growth studies, emphasizing the necessity for advanced land-use and land cover change information for remote sensing optical satellite imagery application [28–30]. Multispectral satellite images have been used as source data for LULC change and water body detection applications since the 1960s [31]. Multispectral remote sensing includes the acquisition of visible, near-infrared, and short-wave infrared images in many broad wavelength bands [32]. Different materials reflect and absorb differently at different wavelengths, and this absorbance and emissivity characteristic are used to detect LULC changes [33].

Multispectral images are primarily applied in detection of urban land-use changes, rather than hyperspectral images [34,35]. Digital data in the form of satellite images enable accurate computing of various LULC categories and help maintain the spatial data infrastructure, which is essential for monitoring urban expansion and for land-use studies [36]. Consequently, RS and GIS data products are effectively used in watershed, town, urban, and regional planning [37]. Since most of the surface runoff modeling and landcover detection parameters are geographic data, integration of RS and GIS techniques is expected to be more effective in evaluating the impacts of urban LULC. GIS has been extensively applied in hydrologic models [27,38,39] because of its spatial analysis function, especially for model data preparation, model input parameters extraction, or model output visualization [39].

The Soil Conservation Service Curve Number (SCS-CN) method, one of the most widely used in rainfall–runoff modeling, was developed by the Natural Resources Conservation Service (SCS), U.S. Department of Agriculture (USDA) [40–42]. According to numerous studies [43–48], the SCS-CN method was developed beyond its original scope and turned into an integral part of simulation models. This method was applied for different landscape structures, soils, and climate conditions [49–53]. These research outputs indicated that the SCS-CN runoff method could be used effectively for large and small watershed areas. In this study, we combined RS and GIS to measure stormwater runoff and establish a relationship between rainfall and the stormwater runoff coefficient (i.e., the ratio of surface runoff to total rainfall). Stormwater runoff coefficient, a crucial parameter in hydrology, is frequently used to examine the impacts of urban LULC, which leads to

urban runoff generation [54]. Stormwater runoff, pollutants management, and subsequent accumulation in soils, surface water, and groundwater pose significant challenges to many Federal and State agencies. These challenges warrant a better assessment of the impacts of suburban growth on runoff changes and local hydrology.

Due to rapid urbanization and its impact on the environment, researchers often concentrate on highly urban areas to detect LULC changes and degradation rather than focusing on suburban areas. Because of population demand and the interest in and need for infrastructural development, suburban land-use is also gradually changing over time, turning into urban areas. Only a limited number of studies have been done on suburban LULC change detection, and no research has been conducted in the selected suburban area. A recent study in this suburban area has revealed high chloride concentration in the impervious zone due to road salt during the winter season [12]. The study area also experienced two significant flood events within a short duration; one happened in March 2010, and another occurred in March 2013 (Figure 1) [55–62]. The 2010 flood event resulted from the combination of the March Nor'easter storm and reservoir management, while the 2013 flood was a precipitation event. The flood duration for 2010 and 2013 was three days and one day, respectively, but the damage amount was massive. The magnitude of these flood events and damages has cost the urban and suburban infrastructure, which led us to investigate the land-use changes and assess the impact of suburban growth on surface runoff.



Figure 1. A glimpse of flood events from 2010 (a,b) and 2013 (c,d) in the conducted research area. Source: 2010 flood [56] and 2013 flood [60].

This study included an integrated approach to estimate the surface runoff and examine suburban growth effects on LULC pattern change. The main objectives are: (a) to detect suburban LULC changes using satellite RS and GIS and to study spatial patterns of suburban growth; (b) to examine the effect of such suburban growth on surface runoff generation; and (c) to detect the most affected area within the urban watershed.

2. Study Area

This study is focused on a suburban municipality (South Kingstown) in southern Rhode Island, USA (Figure 2). According to the definition of ‘suburban’ [63], the population density is usually between 1000–1200 individuals per square kilometer. In our study, the population is slightly lower, i.e., 206.2 per square kilometer according to the 2010 census, than the population for defined suburban areas. The study area is predominantly flat,

low relief, and the annual average rainfall is approximately 1.34 m [62]. Based on bore log data, the groundwater level in this area is 3.12 m from the surface, and the upper part of the aquifer is dominated by sand with some gravel [64,65]. The geology of the aquifer, combined with the shallow groundwater table and the prevalence of impervious surfaces, classifies this system's water as a high-risk area for pollution-induced by surface runoff [65].

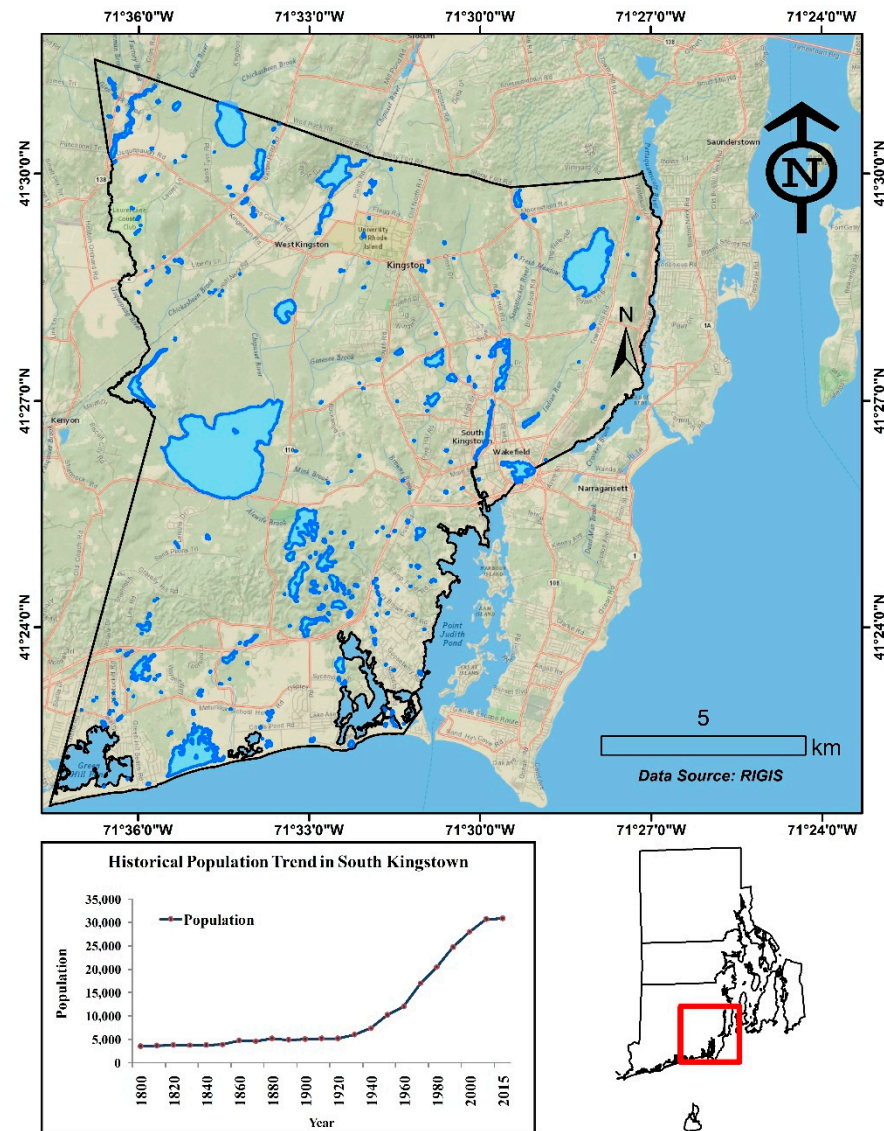


Figure 2. The geographical location for the study site: South Kingstown, RI, USA.

This study used four multispectral (MS) satellite images at 30 m spatial resolution from USGS EarthExplorer [63]. Specifically, to ensure the original image's spectral quality, we used MS imagery, which includes standard red-green-blue (RGB) channels and narrow spectral channels from near- or middle-infrared regions' reflectance spectra [29,30]. Four candidate image scenes were chosen from four different years, and their respective features are presented in Table 1. It is noted that each image scene was radiometrically corrected using a relative radiometric correction method [66] with Erdas Imagine. The scanline error correction was also conducted for the Landsat 7 ETM image. Scanline error correction is required for LANDSAT 7 ETM images except LANDSAT 5 TM. Striping is one of the limitations for LANDSAT 7 ETM images. The striping arises due to the scanline corrector (SLC) failure in 2003 [33,35]. Finally, surface runoff estimates were obtained from these satellite image scenes applying GIS application.

Table 1. General characteristics of four candidate image scenes.

S.No.	Date of Images	Satellite	Sensors	Resolution (m)	Bands	Thermal Band
1.	19 September 1994	LANDSAT-5	TM	30	7	6
2.	14 September 2004	LANDSAT-5	TM	30	7	6
3.	18 September 2014	LANDSAT-7	ETM	30	8	6
4.	9 August 2020	LANDSAT-8	OLI	30	11	10 and 11

3. Methodology

3.1. Surface Runoff Model

In this research, we applied the Soil Conservation Service (SCS) method in rainfall–runoff modeling. The SCS method utilizes several significant factors such as soils, watershed characteristics, i.e., slope, elevation, shape, and land-use over the study area [67,68]. The other two noteworthy factors that affect runoff are rainfall duration and intensity. The SCS-CN model was extensively used to determine the CN, ranging from 0–100 [67]. The estimates of surface runoff depend on the potential retention in the catchment. Surface runoff is largely impacted by three factors, i.e., interception, surface retention, and infiltration, which vary for different soil types. The SCS-CN equation is mathematically represented as Equation (1):

$$Q = \frac{(P - 0.2S)^2}{(P + 0.8S)} \quad (1)$$

Here, Q indicates storm runoff which is estimated from rainfall (P), and S specifies maximum potential storage and is defined as,

$$S = \left(\frac{1000}{CN} \right) - 10 \quad (2)$$

Here, CN indicates the runoff curve number of a hydrologic soil group–landcover complex. Two parameters are required to solve the equation: rainfall (p) and CN. The rainfall data is collected from the National Oceanic and Atmospheric Administration (NOAA). CN is used to estimate the runoff from rainfall, ranging between 30 to 100 based on soil properties of land types (Table 2). In this study, rainfall–runoff depth is estimated for nine different kinds of land type: (1) Agricultural land, (2) Commercial land, (3) Forest, (4) Grass and pasture, (5) Residential, (6) Industrial, (7) Open Space, (8) Parking lot and street, and (9) Water. The permeability characterizes the hydrological soil group (HSG) (A, B, C, D). The infiltration rate is higher in group A (>0.30 in/h or >7.62 mm/h) even when the soil is thoroughly wetted, while group D has the lowest permeability and infiltration rate (0–0.05 in/h or 0.127–0.62 mm/h) for the runoff. Group B (0.15–0.30 in/h or 3.81–7.62 mm/h) and C (0.05–0.15 in/h or 1.27–3.81 mm/h) soils are intermediate between groups A and D. Group A and D consist of sand and clay, respectively. Rango et al. (1983) [68] claimed only a 5% error in land-cover estimates from Landsat data at the basin level and a much higher error at the cell level. A composite CN can be computed for the different land-uses for a watershed using the following equation:

$$CN_c = \frac{CN_1A_1 + CN_2A_2 + \dots + CN_iA_i + \dots + CN_nA_n}{\sum_{i=1}^n A_i} \quad (3)$$

where CN_i is the curve number of area i , A_i is the area of each LULC for area i and n is the number of land uses. In this study, CN is calculated for each land class using ArcGIS 10.6 from the vector soil dataset.

Table 2. General characteristics of four candidate image scenes.

Land Type	A	B	C	D
Agricultural Land	64	75	82	85
Commercial	89	92	94	95
Forest	30	55	70	77
Grass/Pasture	39	61	74	80
Residential	60	74	83	87
Industrial	81	88	91	93
Open Space	49	69	79	84
Parking and paved spaces	98	98	98	98
Water/Wetlands	0	0	0	0

Adapted from 210-VI-TR-55, Second Ed., June 1986 [64].

3.2. Integrated RS-GIS Approach to Surface Runoff Modeling

Integrated RS-GIS approaches are used for surface runoff modeling. The analysis comprises three main parts: (a) derivation of the land class of the study area using RS, (b) hydrological parameter determination applying GIS, and (c) runoff modeling using GIS. For the land class derivation, four MS image scenes were selected from four different years. The land class type and soil information provided the hydrological curve number, one of the key parameters needed for the hydrologic models. Hydrological parameters (directly related to runoff calculation), such as maximum storage, were determined using the curve number. The land-use types were used as independent variables for the proposed methodology. Lastly, the runoff was determined using precipitation and the maximum storage dataset. In the succeeding sub-sections, all three processes are described in detail.

3.2.1. Land-Use and Land Cover Type Using Remote Sensing

We used land-use and land cover patterns for four different years from 1994 to 2020 at the same and almost the same time (Table 2). For all the images, we considered less than 10% cloud cover. Initially, all images were corrected using a common Universal Transverse Mercator (UTM) coordinate system [69]. Every image was then radiometrically corrected according to the Jensen method [67]. Scanline error correction was done for the 2014 images. For the land-use and landcover derivation, supervised classification with a maximum likelihood algorithm was applied [70,71]. The MS image for 2020 was collected from Landsat 8 OLI (Operational Land Imager), and scanline error correction was not required for this image.

A supervised classification method was used for image classification. This method usually requires a priori knowledge of each of the land types. A group of training data sets was collected to identify each of the land types. Four different classification algorithms were available to proceed with the supervised classification. In this study, we applied the maximum likelihood approach for land-use change analysis. The algorithm uses the spectral signature of the pixels from the training dataset to classify the whole image. The spectral signature file used the training information to define the statistics, such as mean and variance of each land type. Every training dataset consists of at least 5 to 10 data points [71]. The more data points represented, the greater the accuracy of the classification. In this study, we collected 12 to 15 data points for each of the land classes. The process was subsequently applied to 1994, 2004, 2014, and 2020 (Figure 3).

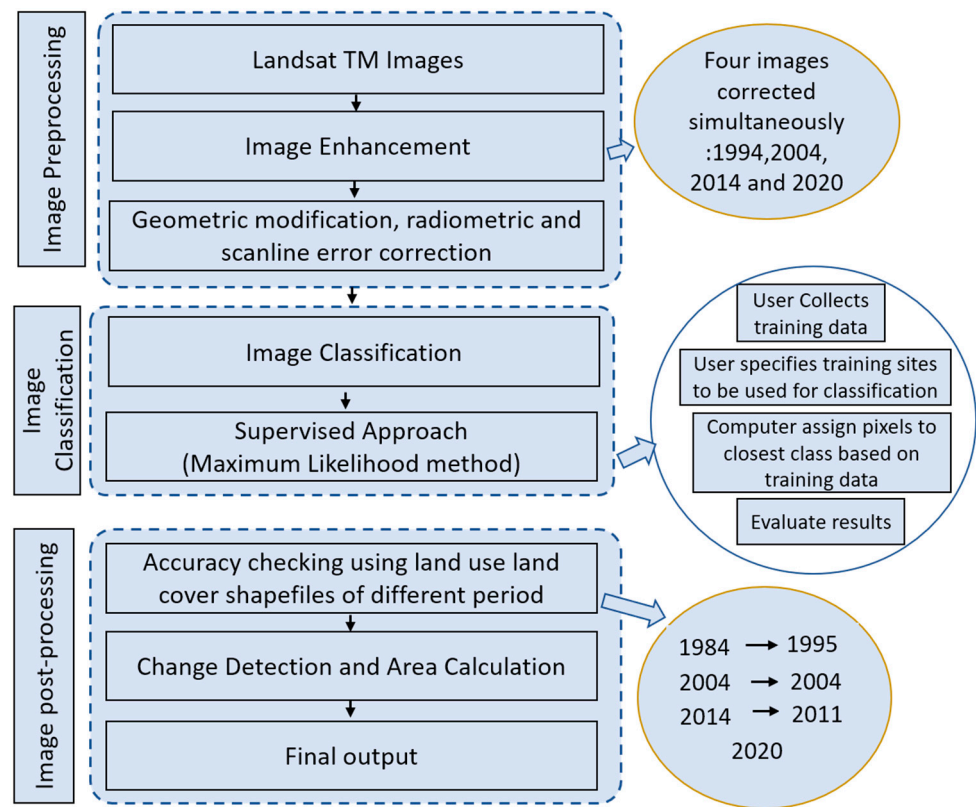


Figure 3. The Process of Land-use and land cover Change Detection.

Every classified image was superimposed by land-use and land cover shapefiles from Anderson land classes to determine the accuracy of the classification [70], which were used to categorize the land use. Land use and land cover vector files are available for 1995, 2004, and 2011 in the Rhode Island Geographic Information System (RIGIS). Therefore, the classified images are evaluated with the publicly available land-use and land cover vector datasets. 1995, 2004, and 2011 data were used to evaluate 1994, 2004, and 2014 land classification. Since the current land-use and land cover shapefile for 2020 is not available, no image accuracy evaluation was done for 2020 land classes.

In this study, residential, commercial, industrial, and parking lot and street areas were considered urban class types as they are also directly related to population growth. A total of nine land-use classes (Table 2) were derived from the images. In terms of using multispectral perspective, three-band combinations: Green (band 2), Red (band 3), and near-infrared (band 4) were used to derive the land classification. A flow chart is presented in Figure 3 to describe the detailed process.

The classified suburban growth image was overlaid with the vector files to calibrate the suburban expansion area. All the raster files were created using 30 m cell size, and this cell size area was calculated for every land class. The town boundary vector file was utilized to detect the suburban expansion for the particular year.

To detect urban expansion in the suburban area, curve number (CN) values were used (Table 2). Table 2 represents the CN value for different land types and hydrologic soil groups.

3.2.2. Hydrogeological Parameter Determination Using GIS

In this step, we prepared soil and precipitation images to generate hydrogeological parameters, and the overall processes are discussed below:

Derivation of Soil Data

The soil data is prepared from a digital soil survey with a detailed soil geographic data level, jointly developed by the Rhode Island Soil Survey and National Cooperative Soil Survey, and was downloaded from the Rhode Island Geographic Information System (RIGIS) [72]. The map data contains detailed information such as hydrological group, shape area, shape length, and soil name. For this study, we applied hydrologic soil group (HSG) (A, B, C, and D) (Figure 4b) information (Table 2) for each land type. All four types of HSG were found in the study area. As shown in Figure 4b, the HSG in group B occupied about 29% (61 sq. km) of the total area. About 22% (48 sq. km) of the total area belonged to group D. However, group A and C occupied approximately 17.7% (37 sq. km) and 9.1% (19 sq. km), respectively. Considering the HSG proportion, the study mainly consisted of a moderate infiltration rate (group B) of 3.81 to 7.62 mm/h. A raster file is then generated for the study area based on the hydrologic group using the runoff curve number (CN) values. The maximum storage of the area was then calculated using the raster calculator.

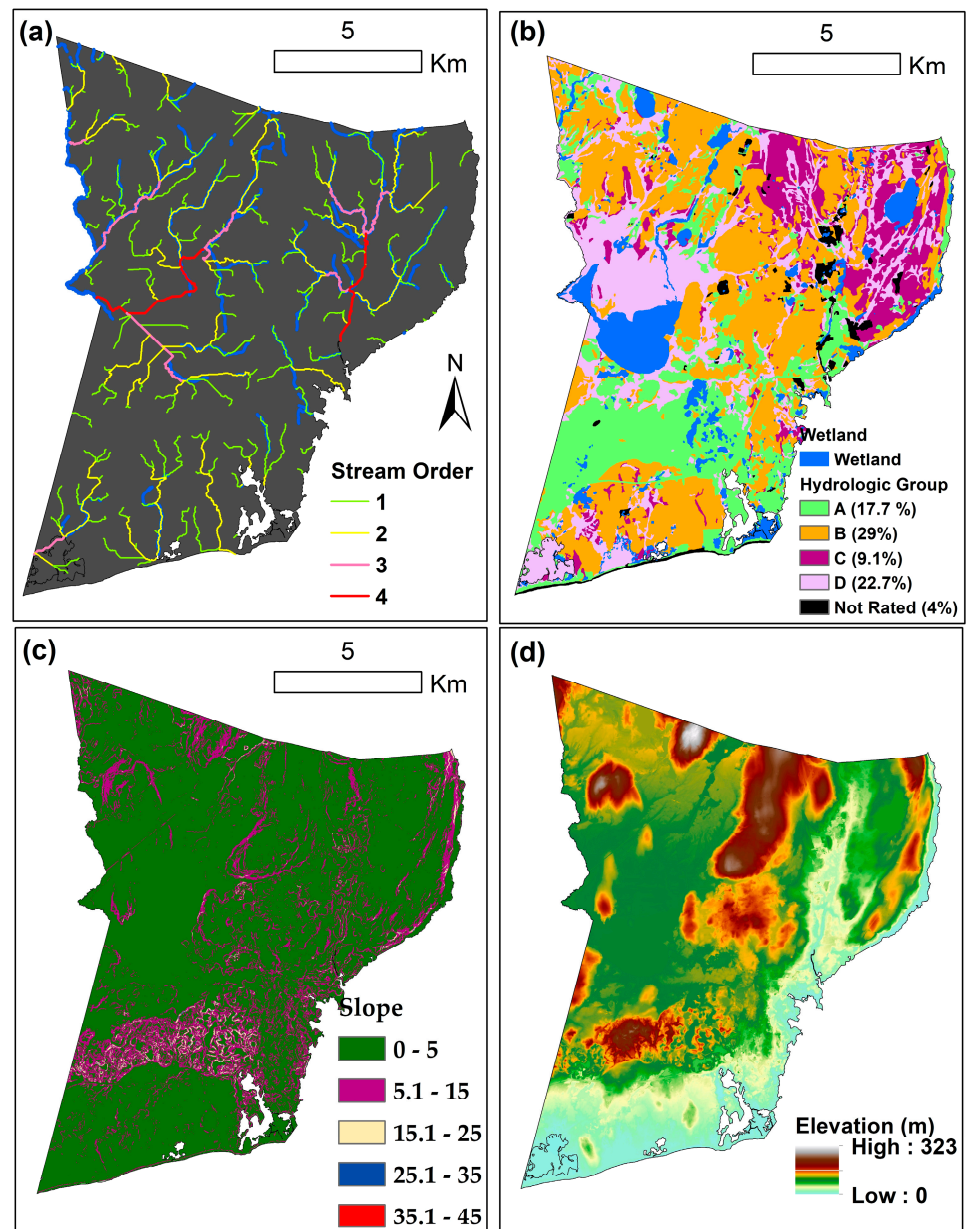


Figure 4. Hydrogeological parameters for the study area: (a) Stream order, (b) Hydrologic soil group (HSG), (c) Slope, (d) Elevation.

Derivation of Slope, Elevation, and Stream Order Data

A slope is an essential parameter of watershed characteristics representing an angle between the inclined ground surface and the horizontal plane. A slope map was produced (Figure 4c) using a DEM with a 30 m resolution for the study area applying the ‘surface’ option from the spatial analyst tool of ArcGIS. The slope map showed the slope variation in degree. About 75% of the area had a slope between (0–5) degree, and 18% of the area had a slope of (5.1–15) degree, mainly in the southern part of the study area. Consequently, elevation (Figure 4d) and stream order (Figure 4a) maps were also developed to represent the overall scenario of the hydrogeological parameter of the study area. This area’s elevation ranges from 0 to 323 m and has predominantly first and second-order streams.

Rainfall Data

Rain data was derived from the Parameter-elevation Regressions on Independent Slopes Model (PRISM) [73–75] climate mapping system. Since only one USGS weather station was available in the study area, there were insufficient neighboring stations to create the spatial distribution of rainfall in a given area. Therefore, the PRISM-derived high-resolution precipitation data were considered for this study. PRISM precipitation products are spatially gridded at 4 km resolution. Elevation is the primary variable that controls the precipitation pattern [76–78]. PRISM data accounts for elevation impacts and, therefore, could be used reliably for this study.

For this study area, 10 PRISM stations are projected and used for the analysis. The kriging application [79] was used to generate the spatial distribution image by assigning average yearly rainfall in the coverage with a 30 m cell size for the raster. Kriging is expressed as:

$$Z_k = \sum_{i=1}^n \lambda_i Z_i \quad (4)$$

where Z_k is an estimate by kriging, λ is a weight for Z_i and Z_i is a variable. The weight is determined to ensure unbiasedness [79].

PRISM data helped to calculate the storage for the entire study area for each of the land classes.

3.2.3. Hydrological Modeling within GIS

We applied GIS for the runoff modeling of this suburban watershed (Figure 5). Multiple images (a land cover image and soil image) were used to construct the CN image. Each area’s CN value was estimated using USDA 1972 [67] standard SCS values (Table 2). Potential maximum storage, S , was derived using map algebra application of GIS for the entire time series. Then, storm runoff depth images were prepared from rainfall, and potential maximum storage images using Equation (1). Four images for 1994, 2004, 2014, and 2020 were created for four different years applying the same methodology. The resulting runoff images were reclassified into runoff ranks. Suburban growth and its development were most prominent in the potential maximum storage images.

We then developed the relationship between rainfall–runoff coefficients for this study area. The runoff coefficient was calculated for each of the selected years’ ten largest storm events based on the rainfall amount. A runoff coefficient curve was then constructed as a function of the flood size. A significant change of the suburban effect based on the runoff coefficient pattern was observed over time.

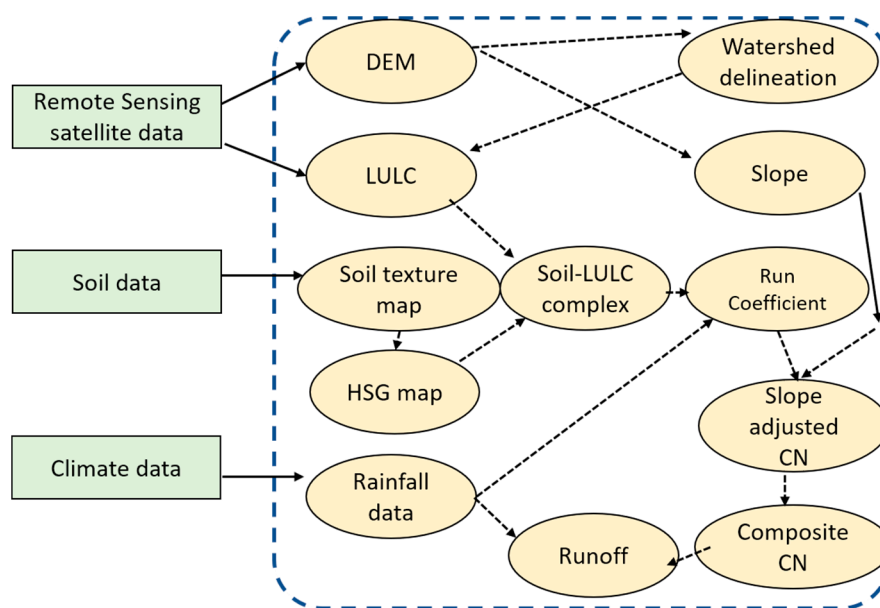


Figure 5. A schematic representation of the geographic information system (GIS) based soil conservation service curve number (SCS-CN) model in estimating the surface runoff.

4. Results and Discussion

4.1. Suburban Growth in the Study Area

Suburban growth represents the expansion of residential, commercial, industrial, and roads and parking lots, and results indicate an increasing trend as shown in Table 3. Land type change detected both areal expansion and reduction. The 36 years analysis results (Table 3) showed that the suburban area expanded by about 68.6% (6564 acres) within this administrative region.

Table 3. Satellite-detected suburban expansion in South Kingstown, Rhode Island.

Land Type	Calculated Area (Acre)		Change Detection of the Area	
	1994	2020	Area (Acre)	%
Urban	9569	16,133	6564	68.6
Agriculture	2684	2814	130	4.8
Forest	18,440	16,934	−1506	−8.2
Grass/Pasture	6662	710	−5952	−89.3

Simultaneously, the agricultural area increased considerably (by approximately 5%), and the forest area decreased by nearly 8.2%. The proportion of urban area to the total land area was 18%, 20.4%, 29%, and 31% in 1994, 2004, 2014, and 2020, respectively. According to land-use change detection, from 1994 to 2004 suburban areas did not expand. Differences in LULC change from 1994 to 2020 from satellite image analysis are presented in Table 3.

In this study, suburban land-use expansion (Figure 6) is the main predictor in analyzing the surface runoff pattern. Suburban growth is directly related to percentage imperviousness. Increasing imperviousness leads to an increase the suburban runoff.

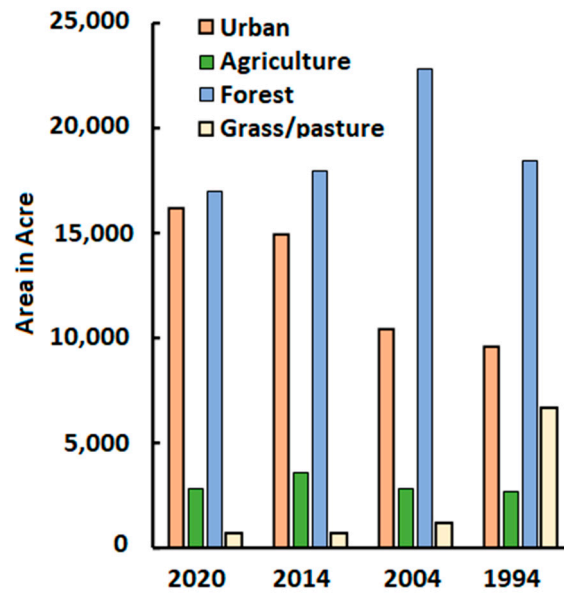


Figure 6. Land type change detection from 1994 to 2020.

In the study area, suburban expansion started from 2000 to 2020 along with considerable population growth [75]. Suburban institutional development also exhibited the overall expansion of the suburban area. For suburban growth, the main driving factor is population growth and residential zone demand [4–6]. The suburban area expanded by 68.6% during this time; if the trend continues, the suburban area will quickly convert to an urban area.

4.2. Impact of Suburban Growth on Surface Runoff

The impact of suburban expansion on surface runoff was examined by comparing the measured runoff volume from 1994 to 2020. With the growth in suburban expansion, runoff is also expanded over time. This study found that suburban growth increased surface runoff. The GIS-based SCS-CN model was used to evaluate the surface runoff for the years 1994, 2004, 2014, and 2020. For each of the years, runoff areas for different runoff depths were calculated. The resulting images of runoff depth showed the runoff depth changes in this area (Figure 7).

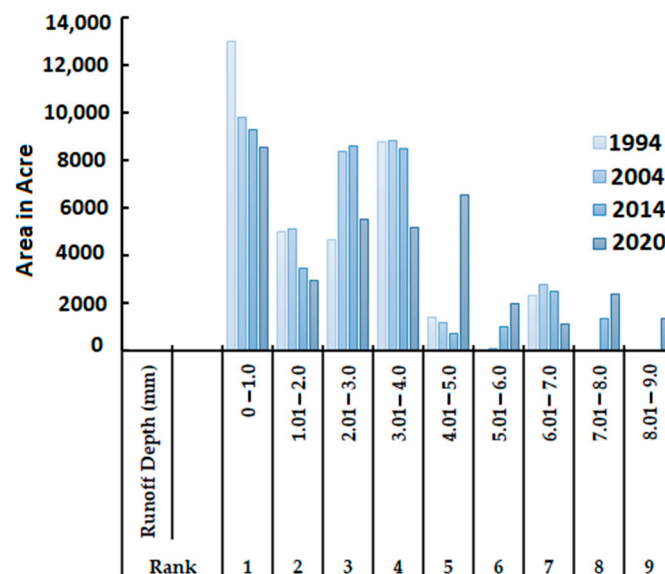


Figure 7. Runoff depth change detection and area from 1994 to 2020.

The spatial distribution of modeled runoff (Figure 8) showed the runoff change in 2014 and 2020 compared to 1984. A moderate runoff depth (Figure 7) and runoff area increased over time in the study area. The runoff increase was relatively low from 1994 to 2004 and higher in 2014; even in 2020, the runoff depth increased significantly (by about 15% on average) compared to 2014 (Figure 7).

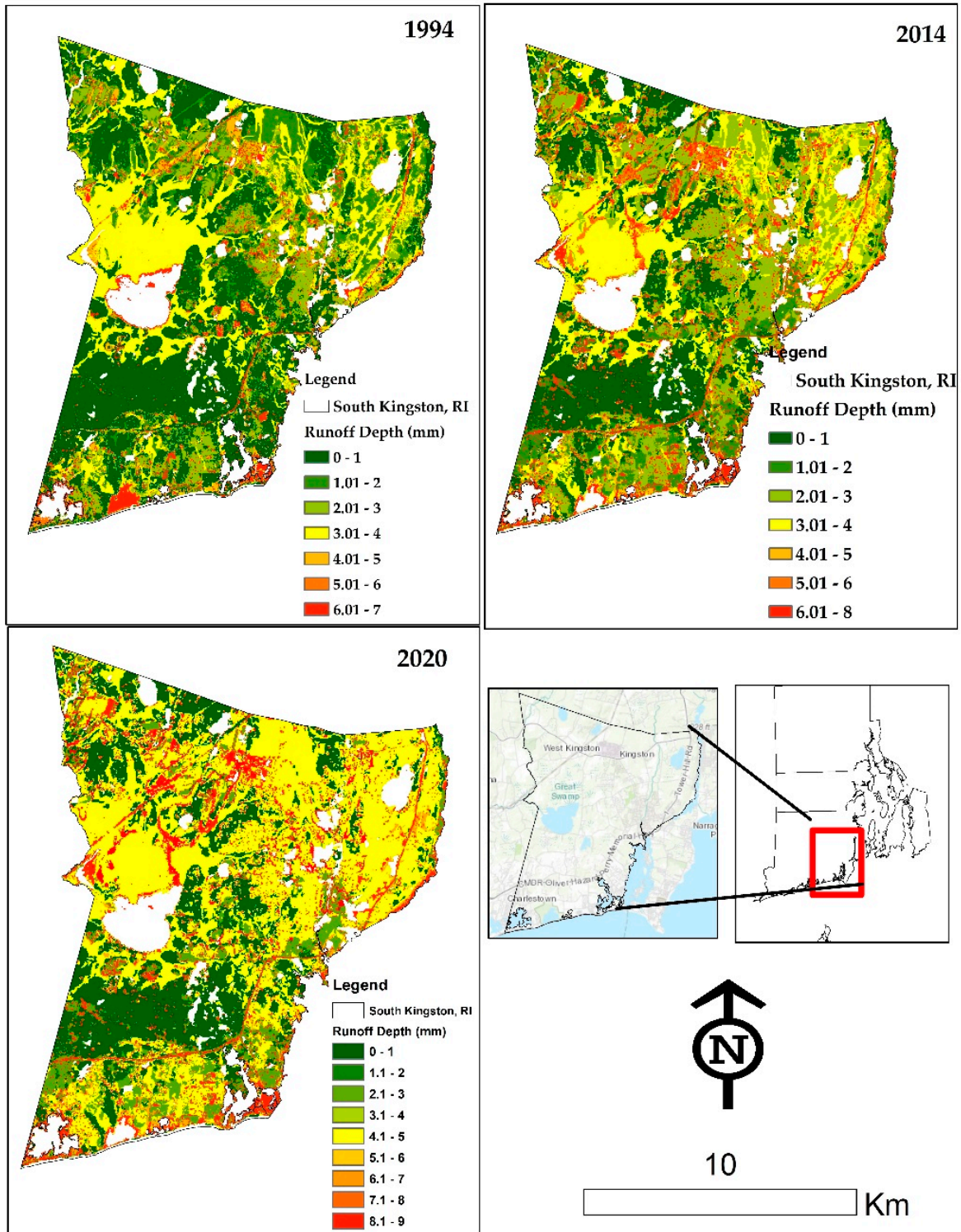


Figure 8. Storm Runoff depth of 2020, 2014 and 1994.

We then ranked runoff from 1 to 9 based on the runoff depth, indicating the lowest runoff depth as rank 1 (i.e., a decrease or no change in runoff depth) and the highest rank as 9 (i.e., zones having the highest runoff depth of 9 mm in 2020). Each of these ranks is a continuous and discontinuous extension expressed with a different color in the raster file for 1994, 2014, and 2020. The yellow color represents the runoff depth of 3 to 4 mm in 1994 and 2014. Noticeably, yellow holds a major portion of the study area in 1994 (17.2% of total area) and 2014 (16.6% of the total area). However, in 2020, the noticeable portion of the site has a runoff depth of 4 to 5 mm, indicating that the area had a higher runoff depth in 2020. In 2020, the maximum runoff depth was reported as 9 mm, which was not observed in the previously investigated years (1994, 2004, and 2014). A visual and detailed interpretation of the study area's areal extent and spatial occurrence was created by aggregating categories 6 to 8 for 2014 (Figure 8). Due to a small amount of suburban growth between 1994 and 2004, the spatial distribution of runoff depth for 2004 did not show much change relative to 1994. The modeled runoff spatial distribution of each of the years (1994, 2014, and 2020) reflected suburban expansion in this area. The land-use classification showed that urban land type for 2020 increased by approximately 8.3% from 2014, and these land changes led to an increase of runoff depth from 2014.

The total area of runoff depth under the ranks increased by around 21.7% from 1994 to 2020. Despite the decrease in rainfall, we still found an increasing trend in runoff depth. This was higher in the northwestern part of the study site. This northwestern area was also becoming more vulnerable, due to expansion in suburban growth and land use. A correlation between the distributed runoff area and the suburban expansion area was examined using the ordinary least square (OLS) tool from the spatial statistical option in ArcGIS. The result showed a strong positive correlation between two mapped patterns with multiple r -values of 0.63 (average) ($p < 0.05$), where the correlation value indicated an increasing trend along with the increasing suburban growth in the study area.

4.3. Impact of Suburban Growth on Rainfall–Runoff Relationship

The runoff coefficient was measured according to the ten highest rainfall events for each of the years. The runoff coefficient range varied based on imperviousness, rainfall depth, duration, and intensity [15]. Figure 9 showed the relationship between rainfall and runoff coefficient for the study area. A higher runoff coefficient was expected when there was more rainfall volume over the suburban area. According to the SCS model, the rainfall and runoff coefficient relationship is governed by maximum potential storage. The impervious zone has low or no potential storage, and the runoff coefficient value showed a strong relationship in these areas. This strong relationship illustrates the effects of suburban growth in this study area. The two dynamic variables are the suburban growth rate and the maximum potential storage. A correlation between the suburban growth rate and the maximum potential storage variables generated $r = 0.45$ in 1994, $r = 0.68$ in 2014 and $r = 0.71$ in 2020. The highest runoff coefficient was 0.51 in 1994, 0.72 in 2014, and 0.97 in 2020. During the entire period from 1994 to 2020, the runoff coefficient increased by about 0.46. This increasing trend indicated that urbanization played a vital role in the rainfall–runoff relationship. Thus, urbanized areas are more prone to increased runoff and flooding events because lower potential storage often implies that the same amount of rainfall may generate more runoff depth depending on imperviousness [13,14]. Furthermore, the land-use change detection showed about 68.6% increased suburban growth from 1994 to 2020 (Table 3). The standard deviation of the runoff coefficient, ranging from 0.16 to 0.021 for these 36 years, indicates suburban growth.

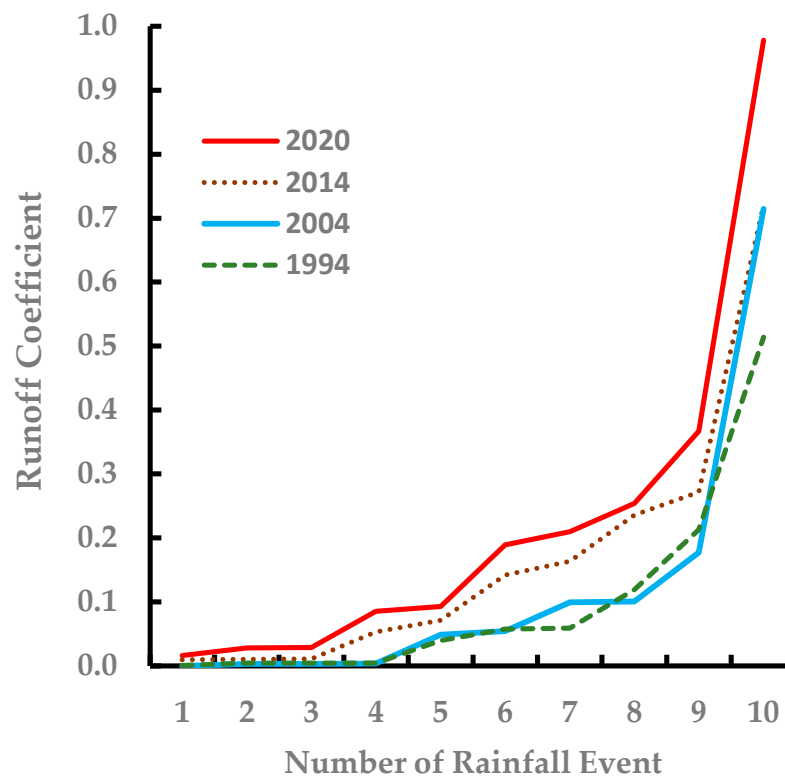


Figure 9. Rainfall–runoff relationship for the study period.

5. Conclusions

We developed an integrated approach using a RS and GIS-based SCS-CN model to assess suburban growth influences in surface runoff. The combined effort of RS-GIS confirms it to be an efficient tool for suburban growth analysis. By applying this methodology, we developed a linkage between suburban growth and surface runoff through spatial analysis, which showed a positive and significant correlation.

Land-use and land cover changes are examined through remote sensing using four different Landsat images applying supervised classification. We emphasized the change detection in the urban land type. The analyzed output showed that urban areas expanded by about 68.6% from 1994 to 2020, whereas forest (decreased by only 8.2%) and agricultural (decreased by only 4.8%) land types showed a little change in this area. Despite this slight change in forest and agriculture, significant urban land change impacted the surface runoff, and this change confirmed suburban growth in suburban areas. The output raster file of land use changes from remote sensing was used as an input parameter along with soil and precipitation in the GIS-based SCS-CN model.

The GIS-based SCS-CN approach was applied to develop the model for estimating runoff for four different years. The significant advantage of employing the GIS application in rainfall–runoff modeling is that more accurate sizing and calculation can be achieved compared to traditional methods. We relied on GIS analysis to detect the suburban growth effect on surface runoff in the study areas. Surface runoff and its areal extension were also examined from the analysis. The modeled output indicated that runoff depth had increased from 2–10% from 1994 to 2020. The spatial distribution of the surface runoff also signifies a moderate to significant effect of suburban growth. Furthermore, the increasing trend of runoff coefficient with time and rainfall events indicates the positive impact of suburban growth.

The integrated approach worked successfully in suburban areas and could arrive at the stormwater quality impacts in this study. Stormwater quality degradation could be the scope of work for further analysis. The two primary factors that were predictors of the surface runoff are rainfall and the hydro group soils (HSG) group. From 1994 to 2020,

both runoff depth and spatial extension of runoff areas enlarged. Due to the increase of suburban expansion in the northwestern part of the study area, the runoff depth primarily increased. This integrated approach is a valuable tool to analyze suburban growth and its impact on surface runoff by developing rainfall–runoff modeling, especially for suburban areas. This research’s final output strongly supports the impact of urbanization impact in this suburban region on surface runoff. Further research should be focused on stormwater management in terms of quality and quantity to minimize the future environmental impact in suburban areas.

Author Contributions: For this research, K.J. developed the research framework, designed and carried out the analysis of results, and wrote the original paper. S.M.P. contributed to the interpretation of results, resources, supervision, project administration. M.A.E.B. conceptualization, figures preparation, interpretation of results, writing, review & editing and contributed to the development of the paper. All authors have read and agreed to the published version of the manuscript.

Funding: The research study is funded by the Rhode Island Department of Transportation, SPR-234-2362, and the University of Rhode Island.

Institutional Review Board Statement: Not Applicable.

Informed Consent Statement: Not Applicable.

Data Availability Statement: Data sharing not applicable.

Acknowledgments: Authors are thankful to the Rhode Island Department of Transportation (RIDOT) for the project fund. We also thank Arthur Gold and Yeqiao Wang, Professors of the University of Rhode Island, for their valuable comments and recommendations.

Conflicts of Interest: The authors declare no conflict of interest.

References

1. Grimm, N.B.; Faeth, S.H.; Golubiewski, N.E.; Redman, C.L.; Wu, J.; Bai, X.; Briggs, J.M. Global Change and the Ecology of Cities. *Science* **2008**, *319*, 756–760. [CrossRef] [PubMed]
2. Pradhanang, S.; Jahan, K. *Urban Water Security for Sustainable Cities in the Context of Climate Change*; Chapter 14, Water, Climate and Sustainability; John Wiley & Sons, Inc.: Hoboken, NJ, USA, 2021; pp. 213–224. [CrossRef]
3. Hegazy, I.R.; Kaloop, M.R. Monitoring urban growth and land use change detection with GIS and remote sensing techniques in Daqahlia governorate Egypt. *Int. J. Sustain. Built Environ.* **2015**, *4*, 117–124. [CrossRef]
4. UN-HABITAT (United Nations Human Settlement Programme). *The State of the African Cities 2008—A Framework for Addressing Urban Challenges in Africa*. Nairobi; United Nations Human Settlements Programme, Oxford University Press: Oxford, UK, 2008.
5. Sankhala, S.; Singh, B. Evaluation of urban sprawl and land use land cover change using remote sensing and GIS techniques: A case study of Jaipur City, India. *J. Int. J. Emerg. Technol. Adv. Eng.* **2014**, *4*, 66–72.
6. Abustan, I.; Sulaiman, A.H.; Wahid, N.A.; Baharuddin, F. Determination of rainfall-runoff characteristics in an urban area: Sungai kerayong catchment, Kuala Lumpur. In Proceedings of the 11th International Conference on Urban Drainage, Edinburgh, UK, 31 August–5 September 2008; Available online: <https://citeseerx.ist.psu.edu/viewdoc/download?doi=10.1.1.517.1745&rep=rep1&type=pdf> (accessed on 11 March 2021).
7. Weng, Q. Modeling urban growth effects on surface runoff with the integration of remote sensing and GIS. *J. Environ. Manag.* **2001**, *28*, 737–748. [CrossRef] [PubMed]
8. Kibler, D.F. (Ed.) *Urban Stormwater Hydrology*; American Geophysical Union: Washington, DC, USA, 1982.
9. Goudie, A. *The Human Impact on the Natural Environment*, 3rd ed.; The MIT Press: Cambridge, MA, USA, 1990.
10. Komrad, C.P. Effect of Urban Development on Floods. U.S. Geological Survey 2003, USGS Fact Sheet FS-076-03. Available online: <https://pubs.usgs.gov/fs/fs07603/pdf/fs07603.pdf> (accessed on 11 March 2021).
11. Rogger, M.; Agnoletti, M.; Alaoui, A.; Bathurst, J.C.; Bodner, G.; Borga, M.; Chaplot, V.; Gallart, F.; Glatzel, G.; Hall, J.; et al. Land use change impacts on floods at the catchment scale: Challenges and opportunities for future research. *Water Resour. Res.* **2017**, *53*, 5209–5219. [CrossRef]
12. Jahan, K.; Pradhanang, S. Predicting Runoff Chloride Concentrations in Suburban Watersheds Using an Artificial Neural Network (ANN). *J. Hydrol.* **2020**, *7*, 80. [CrossRef]
13. Niemczynowicz, J. Urban hydrology and water management—Present and future challenges. *Urban Water* **1999**, *1*, 1–14. [CrossRef]
14. Fletcher, T.; Andrieu, H.; Hamel, P. Understanding, management and modelling of urban hydrology and its consequences for receiving waters: A state of the art. *Adv. Water Resour.* **2013**, *51*, 261–279. [CrossRef]

15. Isah, T. Remote Sensing Studies on Urban Change Detections. *J. Int. J. Comput. Sci. Inf. Technol. Res.* **2015**, *3*, 62–71. Available online: www.researchpublish.com (accessed on 11 March 2021).
16. Oyinloye, R.O.; Adesina, F.A. Some aspect of the growth of Ibadan and their Implications for socio-economic development. *J. Ife Soc. Sci. Rev.* **2006**, *20*, 113–120.
17. McGrane, S.J. Impacts of urbanisation on hydrological and water quality dynamics, and urban water management: A review. *Hydrol. Sci. J.* **2016**, *61*, 2295–2311. [[CrossRef](#)]
18. Ehlers, M.; Jadcowski, M.A.; Howard, R.R.; Brostuen, D.E. Application of SPOT data for regional growth analysis and local planning. *J. Photogramm. Eng. Remote Sens.* **1990**, *56*, 175–180.
19. Treitz, P.M.; Howard, P.J.; Gong, P. Application of satellite and GIS technologies for land-cover and land-use mapping at the rural-urban fringe: A case study. *J. Photogramm. Eng. Remote Sens.* **1992**, *58*, 439–448.
20. Harris, P.M.; Ventura, S.J. The integration of geographic data with remotely sensed imagery to improve classification in an urban area. *J. Photogramm. Eng. Remote Sens.* **1995**, *61*, 993–998.
21. Yeh, A.G.O.; Li, X. Urban growth management in the Pear River delta—An integrated remote sensing and GIS approach. *J. ITC J.* **1996**, *1*, 77–85.
22. Yeh, A.G.O.; Li, X. An integrated remote sensing and GIS approach in the monitoring and evaluation of rapid urban growth for sustainable development in the Pearl River Delta, China. *Int. Plan. Stud.* **1997**, *2*, 193–210. [[CrossRef](#)]
23. Pandey, A.; Sahu, A.K. Generation of curve number using Remote Sensing and Geographic information system. *J. Geospat. World* **2009**. Available online: <https://www.geospatialworld.net/article/generation-of-curve-number-using-remote-sensing-and-geographic-information-system/> (accessed on 11 March 2021).
24. Gajbhiye, S. Estimation of Surface Runoff Using Remote Sensing and Geographical Information System. *J. Sci. Technol.* **2015**, *8*, 113–122. [[CrossRef](#)]
25. Engman, E.T.; Gurney, R.J. Remote sensing in hydrology. In *Remote Sensing Application Series*; xiv 225; Chapman & Hall: London, UK, 1991.
26. Drayton, R.S.; Wilde, B.M.; Harris, J.H.K. Geographic information system approach to distributed modeling. *J. Hydrol. Process.* **1992**, *6*, 36–368.
27. Mattikalli, N.M.; Devereux, B.J.; Richards, K.S. Prediction of river discharge and surface water quality using an integrated geographic information system approach. *J. Int. J. Remote Sens.* **1996**, *17*, 683–701. [[CrossRef](#)]
28. Radke, J.; Andra, S.; Al-Kofani, O.; Roysan, B. Image change detection algorithms: A systematic survey. *J. IEEE Trans. Image Process.* **2005**, *14*, 291–307. [[CrossRef](#)]
29. Bhuiyan, A.E.; Witharana, C.; Liljedahl, A.K.; Jones, B.M.; Daanen, R.; Epstein, H.E.; Kent, K.; Griffin, C.G.; Agnew, A. Understanding the Effects of Optimal Combination of Spectral Bands on Deep Learning Model Predictions: A Case Study Based on Permafrost Tundra Landform Mapping Using High Resolution Multispectral Satellite Imagery. *J. Imaging* **2020**, *6*, 97. [[CrossRef](#)]
30. Bhuiyan, A.E.; Witharana, C.; Liljedahl, A.K. Use of Very High Spatial Resolution Commercial Satellite Imagery and Deep Learning to Automatically Map Ice-Wedge Polygons across Tundra Vegetation Types. *J. Imaging* **2020**, *6*, 137. [[CrossRef](#)]
31. Nagne, A.D.; Dhupal, R.K.; Vibhute, A.D.; Nalawade, B.D.; Kale, K.V.; Mehrotra, S.C. Advantages in Land use classification of urban areas from Hyperspectral data. *Int. J. Eng. Tech.* **2018**, *4*. Available online: <http://www.ijetjournal.org> (accessed on 11 March 2021).
32. Witharana, C.; Bhuiyan, M.A.E.; Liljedahl, A.K. Big Imagery and high-performance computing as resources to understand changing Arctic polygonal tundra. *Int. Arch. Photogramm.* **2020**, *44*, 111–116. [[CrossRef](#)]
33. Science Mission Directorate. “Wave Behaviors” NASA Science. *J. Natl. Aeronaut. Space Adm.* **2010**. Available online: http://science.nasa.gov/ems/03_behaviors (accessed on 11 March 2021).
34. Witharana, C.; Bhuiyan, M.A.E.; Liljedahl, A.K.; Kanevskiy, M.; Epstein, H.E.; Jones, B.M.; Daanen, R.; Griffin, C.G.; Kent, K.; Jones, M.K.W. Understanding the synergies of deep learning and data fusion of multispectral and panchromatic high resolution commercial satellite imagery for automated ice-wedge polygon detection. *ISPRS J. Photogramm. Remote Sens.* **2020**, *170*, 174–191. [[CrossRef](#)]
35. Mohanrajan, S.N.; Loganathan, A.; Manoharan, P. Survey on Land Use/Land Cover (LU/LC) change analysis in remote sensing and GIS environment: Techniques and Challenges. *Environ. Sci. Pollut. Res.* **2020**, *27*, 29900–29926. [[CrossRef](#)] [[PubMed](#)]
36. Mukherjee, S. Land use maps for conservation of ecosystems. *J. Geog. Rev. India* **1987**, *3*, 23–28.
37. Sharma, S.K.; Gajbhiye, S.; Nema, R.K.; Tignath, S. Assessing vulnerability to soil erosion of a watershed of tons River basin in Madhya Pradesh using Remote sensing and GIS. *J. Int. J. Environ Res Dev* **2014**, *4*, 153–164.
38. Berry, J.K.; Sailor, J.K. Use of a Geographic Information System for storm runoff prediction from small urban watersheds. *J. Environ. Manag.* **1987**, *11*, 21–27. [[CrossRef](#)]
39. Dongquan, Z.; Jining, C.; Haozheng, W.; Qingyuan, T.; Shangbing, C.; Zheng, S. GIS-based urban rainfall-runoff modeling using an automatic catchment-discretization approach: A case study in Macau. *Environ. Earth Sci.* **2009**, *59*, 465–472. [[CrossRef](#)]
40. Mishra, S.K.; Pandey, A.; Singh, V.P. Special Issue on Soil Conservation Service Curve Number (SCS-CN) Methodology. *J. Hydrol. Eng.* **2012**, *17*, 1157. [[CrossRef](#)]
41. Singh, P.K.; Mishra, S.K.; Berndtsson, R.; Jain, M.K.; Pandey, R.P. Development of a Modified SMA Based MSCS-CN Model for Runoff Estimation. *Water Resour. Manag.* **2015**, *29*, 4111–4127. [[CrossRef](#)]

42. Vojtek, M.; Vojteková, J. GIS-based Approach to Estimate Surface Runoff in Small Catchments: A Case Study. *Quaest. Geogr.* **2016**, *35*, 97–116. [CrossRef]
43. Soulis, K.X.; Valiantzas, J.D. SCS-CN parameter determination using rainfall-runoff data in heterogeneous watersheds. The two-CN system approach. *J. Hydrol. Earth Syst. Sci. Discuss.* **2011**, *8*, 8963–9004.
44. Mishra, S.K.; Singh, V.P. Long-term hydrological simulation based on the Soil Conservation Service curve number. *Hydrol. Process.* **2004**, *18*, 1291–1313. [CrossRef]
45. Soulis, K.X.; Dercas, N. Development of a GIS-based spatially distributed continuous hydrological model and its first application. *J. Water Int.* **2007**, *32*, 177–192. [CrossRef]
46. Zhan, X.Y.; Huang, M.L. ArcCN-Runoff: An ArcGIS tool for generating curve number and runoff maps. *J. Environ. Model. Softw.* **2004**, *19*, 875–879. [CrossRef]
47. Moretti, G.; Montanari, A. Inferring the flood frequency distribution for an ungauged basin using a spatially distributed rainfall-runoff model. *Hydrol. Earth Syst. Sci.* **2008**, *12*, 1141–1152. [CrossRef]
48. Adornado, H.A.; Yoshida, M. GIS-based watershed analysis and surface runoff estimation using curve number (C.N.) value. *J. Environ. Hydrol.* **2010**, *18*, 1–10.
49. Wilcox, B.P.; Rawls, W.J.; Brakensiek, D.L.; Wight, J.R. Predicting runoff from Rangeland Catchments: A comparison of two models. *Water Resour. Res.* **1990**, *26*, 2401–2410. [CrossRef]
50. Holman, I.P.; Hollis, J.M.; Bramley, M.E.; Thompson, T.R.E. The contribution of soil structural degradation to catchment flooding: A preliminary investigation of the 2000 floods in England and Wales. *Hydrol. Earth Syst. Sci.* **2003**, *7*, 755–766. [CrossRef]
51. Romero, P.; Castro, G.; Gomez, J.A.; Fereres, E. Curve number values for olive orchards under different soil management. *J. Soil Sci. Soc. Am. J.* **2007**, *71*, 1758–1769. [CrossRef]
52. Tedela, N.H.; McCutcheon, S.C.; Rasmussen, T.C.; Hawkins, R.H.; Swank, W.T.; Campbell, J.L.; Adams, M.B.; Jackson, R.; Tollner, E.W. Runoff curve numbers for 10 small forested watersheds in the mountains of the eastern United States. *J. Hydrol. Eng.* **2012**, *17*, 1188–1198. [CrossRef]
53. Nagarajan, M.; Basil, G. Remote sensing- and GIS-based runoff modeling with the effect of land-use changes (a case study of Cochin corporation). *Nat. Hazards* **2014**, *73*, 2023–2039. [CrossRef]
54. Pandit, A.; Gopalakrishnan, G. Estimation of annual storm runoff coefficients by continuous simulation. *J. Irrig. Drain. Eng.* **1996**, *122*, 211–220. [CrossRef]
55. USGS. *Elevation of the March–April 2010 Flood High Water in Selected River Reaches in Rhode Island* by Phillip, J. Zarriello and Gardener, C. Bent; U.S. Department of the Interior. U.S. Geological Survey: Reston, VA, USA, 2011. Available online: <https://pubs.usgs.gov/of/2011/1029/pdf/ofr2011-1029-508.pdf> (accessed on 11 March 2021).
56. Kenyon Grist Mill. Flood 2010: Photo Documentary (Before, During, and After). All Content Copyright—Official Website of Kenyon Grist Mill LLC 21 Glen Rock Road/P.O. Box 221 West Kingston, RI 02892. 2013. Available online: <https://www.kenyongristmill.com/flood2010.html> (accessed on 11 March 2021).
57. The Independent. Towns, Residents Close to Recover from Historic Flood by Chris Church. 2011. Available online: https://www.independentri.com/local/article_71f7559f-a7ec-537d-b380-80ac5e5c3ddb.html (accessed on 11 March 2021).
58. SRI. A Look Back at the Flood of the Century. Southern Rhode Island Newspaper. 2011. Available online: https://www.ricentral.com/a-look-back-at-the-flood-of-the-century/article_c8e44c9d-a7f9-59f8-ac2b-f345b5f0e0a9.html (accessed on 11 March 2021).
59. Gorman, G. Rhode Island Flood Zones-South Kingstown RI Real Estate Has Them too. Rhode Island Coastal Real Estate. 2012. Available online: https://www.rihousehunt.com/ri-blog/rhode-island-flood-zones-south-kingstown-ri-real-estate-has-them-too/?doing_wp_cron=1614615852.4240589141845703125000 (accessed on 11 March 2021).
60. The Independent. Heavy Rains Brings Flooding, Road Closures. Reporter Stephen Greenwell. 2014. Available online: https://www.independentri.com/independents/south_county/article_35880c91-006d-5e2b-b32b-af311135fe9e.html (accessed on 11 March 2021).
61. Patch the Community Corner. Flash Flood Watch in Narragansett and South Kingstown by Erin Tiernan. Community Corner. 2013. Available online: <https://patch.com/rhode-island/narragansett/flash-flood-watch-in-narragansett-and-south-kingstown> (accessed on 11 March 2021).
62. ECO RI News. Rising Waters Threaten Region’s Cultural Treasures. ECO RI News. 2015. Available online: <https://www.ecori.org/climate-change/2015/1/5/rising-waters-threaten-regions-culture> (accessed on 11 March 2021).
63. USDA. Economic Research Service Using Data from U.S. Census Bureau. 2013. Available online: <https://www.ers.usda.gov/data-products/> (accessed on 11 March 2021).
64. U.S. Climate Data. U.S. Climate Data 2021 | Version 3.0 | by Your Weather Service. 2019. Available online: <https://www.usclimatedata.com/> (accessed on 11 March 2021).
65. South Kingstown Source of Water Assessment (SKSWA), University of Rhode Island Cooperative Extension. 2003. Available online: http://cels.uri.edu/rinemo/assessments/sk_source_water_assesment.pdf (accessed on 11 March 2021).
66. USGS Earth Explorer Landsat Archive (1980–2019). Available online: <https://earthexplorer.usgs.gov> (accessed on 10 February 2019).
67. Jensen, J.R. *Introductory Digital Image Processing: A Remote Sensing Perspective*, 2nd ed.; Prentice-Hall: Hoboken, NJ, USA, 1996.
68. USDA—Soil Conservation Service. *National Engineering Handbook*; Sec. 4. Hydrology; USDA: Washington, DC, USA, 1972.
69. Rango, A.; Feldman, A.; George, T.S.; Ragan, R.M. Effective use of landsat data in hydrologic models. *JAWRA J. Am. Water Resour. Assoc.* **1983**, *19*, 165–174. [CrossRef]

70. Camps-Valls, G.; Tuia, D.; Gómez-Chova, L.; Jiménez, S.; Malo, J. Remote Sensing Image Processing. *Synth. Lect. Image Video Multimedia Process.* **2011**, *5*, 1–192. [[CrossRef](#)]
71. Hütt, C.; Koppe, W.; Miao, Y.; Bareth, G. Best Accuracy Land Use/Land Cover (LULC) Classification to Derive Crop Types Using Multitemporal, Multisensor, and Multi-Polarization SAR Satellite Images. *Remote Sens.* **2016**, *8*, 684. [[CrossRef](#)]
72. Samaniego, L.; Schulz, K. Supervised Classification of Agricultural Land Cover Using a Modified k-NN Technique (MNN) and Landsat Remote Sensing Imagery. *Remote Sens.* **2009**, *1*, 875–895. [[CrossRef](#)]
73. Anderson, J.R.; Hardy, E.E.; Roach, J.T.; Witmer, R.E. *A Land Use and Land Cover Classification for Use with Remote Sensor Data*; (USGS Professional Paper 964); Government Printing Oce: Washington, DC, USA, 1976. [[CrossRef](#)]
74. USDA. Urban Hydrology for Small Watershed TR-55. In *210-VI-TR-55*, 2nd ed.; USDA: Washington, DC, USA, 1986.
75. Daly, C. Guidelines for assessing the suitability of spatial climate data sets. *Int. J. Clim.* **2006**, *26*, 707–721. [[CrossRef](#)]
76. Bhuiyan, M.A.E.; Yang, F.; Biswas, N.K.; Rahat, S.H.; Neelam, T.J. Machine Learning-Based Error Modeling to Improve GPM IMERG Precipitation Product over the Brahmaputra River Basin. *Forecasting* **2020**, *2*, 14. [[CrossRef](#)]
77. Bhuiyan, M.A.; Nikolopoulos, E.I.; Anagnostou, E.N. Machine learning-based blending of satellite and reanalysis precipitation datasets: A multiregional tropical complex terrain evaluation. *J. Hydrometeorol.* **2019**, *20*, 2147–2161. [[CrossRef](#)]
78. Bhuiyan, M.A.E.; Nikolopoulos, E.I.; Anagnostou, E.N.; Quintana-Seguí, P.; Barella-Ortiz, A. A nonparametric statistical technique for combining global precipitation datasets: Development and hydrological evaluation over the Iberian Peninsula. *Hydrol. Earth Syst. Sci.* **2018**, *22*, 1371–1389. [[CrossRef](#)]
79. Journel, A.G.; Huijbregts, C.J. *Mining Geostatistics*; Academic Press: Cambridge, MA, USA, 1978; 600p.